



In Situ Local Temperature Mapping in Microscopy Nano-Reactors with Luminescence Thermometry

Ilse K. van Ravenhorst^{+, [a]}, Robin G. Geitenbeek^{+, [a, c]}, M. J. van der Eerden,^[a] J. Tijn van Omme,^[b] H. Hugo Pérez Garza,^[b] Florian Meirer,^[a] Andries Meijerink,^[c] and Bert M. Weckhuysen^{*[a]}

In situ and *operando* experiments play a crucial role in understanding the mechanisms behind catalytic processes. In these experiments it is important to have precise control over pressure and temperature. In this work, we use luminescence thermometry to map the temperature distribution in a 300 μm microelectromechanical system nano-reactor with a resolution of ca. 10 μm . These measurements showed a temperature gradient between the center and edge of the heater of ca.

200 °C (at $T_{\text{set}} = 600$ °C) in vacuum and, in addition, a large offset of the local temperature of ca. 100 °C (at $T_{\text{set}} = 600$ °C) in a non-vacuum (*i.e.*, air, He and H_2) environment. The observed temperature heterogeneities can explain differences observed in the reduction behavior of Co-based Fischer-Tropsch synthesis catalyst particles at different locations in the nano-reactor as determined by scanning transmission X-ray microscopy.

Introduction

Catalysis is widely used in numerous synthesis processes, from converting car's exhaust gasses over creating the bulk chemicals to producing functional materials and making transportation fuels, such as gasoline and kerosene. In order to create more efficient catalysts, knowledge about the mechanisms that determine efficiency and selectivity are of great importance. Therefore, *in situ* or *operando* spectroscopy and microscopy experiments, that is experiments at laboratory conditions that are as close to industrial conditions as possible, are very important to understand the mechanisms involved. The challenge to replicate industrially relevant conditions (*e.g.* $T > 500$ °C and $P > 50$ bar) on the lab-scale has triggered extensive work in the field of reactor design for *in situ* and *operando* (micro-)spectroscopy.^[1,2] However, depending on the

system and reaction of interest, often a compromise has to be made while striving for investigation of catalytic processes as close as possible to realistic industrial conditions but are hampered by the intrinsic limitations of the experimental setup.

A specific example of a catalyst system where significant efforts have been made to achieve industrial conditions during lab experiments^[3-8] is the Fischer-Tropsch synthesis (FTS), which is a heterogeneous surface polymerization reaction.^[5,9-12] It hydrogenates synthesis gas, a mixture of H_2 and CO, into long-chain hydrocarbons over supported metal catalysts, thereby producing high-purity chemicals and fuels from sources other than crude oil. Additionally, the selectivity towards alkanes, alkenes and alcohols can be tuned by altering the catalyst composition or reaction conditions.^[13,14] The potential of this versatile reaction has resulted in extensive research using traditional spectroscopic techniques, *e.g.* Raman, UV-Vis and FT-IR spectroscopy.^[15-17] These techniques provide valuable insight on the organic part of the catalytic reaction (*e.g.* products and intermediates). However, information on the inorganic materials (*e.g.* catalyst and support) is also vital for the complete understanding of structure-performance relations in catalysis. Here, X-ray spectroscopy can play an important role. For instance, by combining X-ray absorption spectroscopy with Raman spectroscopy, bulk studies of catalysts have been performed which can correlate short-range order, valence state and local geometry of the metals to product formation and reaction intermediates.^[18-20] Although these results are insightful, detailed information on the single catalyst particle level is still lacking. Especially hydrocarbon deposition or coke formation on the single particle level could reveal valuable information since it is believed that this is one of the main reasons for catalyst deactivation.^[21-23]

A promising method for the investigation of both organic and inorganic parts of a catalyst system on the single particle level is scanning transmission X-ray microscopy (STXM), especially in combination with mass spectrometry (MS) or gas chromatography (GC).^[24] STXM is a so-called micro-spectroscopy

[a] I. K. van Ravenhorst,⁺ Dr. R. G. Geitenbeek,⁺ M. J. van der Eerden, Dr. F. Meirer, Prof. Dr. B. M. Weckhuysen
Inorganic Chemistry and Catalysis Debye Institute for Nanomaterials Science

Utrecht University

Universiteitsweg 99, 3584 CG Utrecht (The Netherlands)

E-mail: b.m.weckhuysen@uu.nl

[b] J. Tijn van Omme, Dr. H. H. Pérez Garza

DENSolutions B.V.

Informaticalaan 12, 2628 ZD Delft (The Netherlands)

[c] Dr. R. G. Geitenbeek,⁺ Prof. Dr. A. Meijerink

Condensed Matter and Interfaces

Debye Institute for Nanomaterials Science Utrecht Universiteit

Princetonplein 1, 3584 CC Utrecht (The Netherlands)

[†] These authors contributed equally to this work.



Supporting information for this article is available on the WWW under <https://doi.org/10.1002/cctc.201900985>



This publication is part of a Special Collection on "Advanced Microscopy and Spectroscopy for Catalysis". Please check the ChemCatChem homepage for more articles in the collection.



© 2019 The Authors. Published by Wiley-VCH Verlag GmbH & Co. KGaA. This is an open access article under the terms of the Creative Commons Attribution Non-Commercial License, which permits use, distribution and reproduction in any medium, provided the original work is properly cited and is not used for commercial purposes.

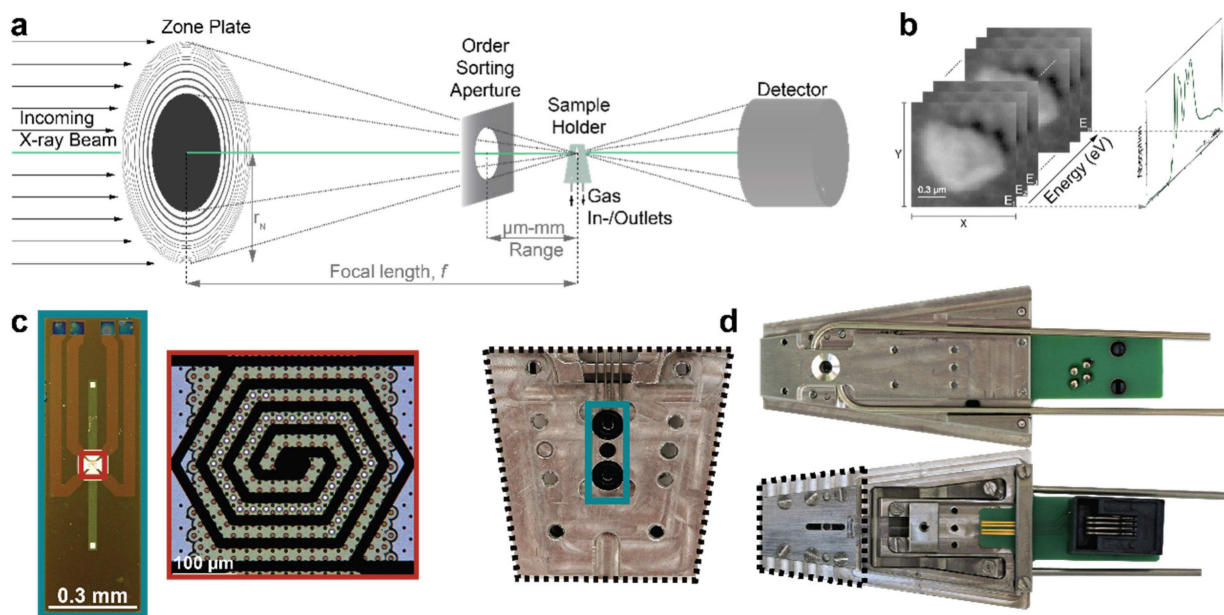


Figure 1. a) A schematic representation of the pathway of soft X-rays in scanning transmission X-ray microscopy (STXM). b) The sample is raster scanned in order to create a point-by-point image in which each point contains a full X-ray absorption spectrum (XAS). c) Microelectromechanical system (MEMS) nano-reactor^[27] and a zoom-in of the resistive Pt heater (red rectangle) spiral ($D = 300 \mu\text{m}$) located in the middle of an electron-transparent window. Within the heated area there are smaller electron-transparent windows with $7 \mu\text{m}$ in diameter and 15 nm thick SiN_x . d) The back and front of the reactor holder and a zoom-in of the front bottom (black dashed line). The front of the holder displays the top plate, which holds the nano-reactor in place, and the electrical connection for the resistance temperature control. The zoom-in shows the two O-rings around the in- and outlet for the gasses, to ensure a leak tight gas connection, and the four needles for temperature control. The blue rectangle indicates the location for the nano-reactor.

technique, which combines microscopy with X-ray absorption spectroscopy and allows studying a wide variety of chemical elements by their X-ray absorption near edge structure (XANES, Figure 1a and 1b) including carbon in the organic fraction of the catalytic process. STXM typically uses a Fresnel zone plate to focus monochromatic X-rays. The focus distance, f (Figure 1a), is dependent on the Fresnel zone plate diameter and the wavelength of the incident radiation. In addition, an order sorting aperture (OSA, Figure 1a) is required to select only first order diffracted light, resulting in a small working distance for STXM experiments [$300\text{--}500 \mu\text{m}$ for the carbon K-edge (290 eV)]. Consequently, no conventional heating sources, such as ovens and heat guns, can be exploited for *in situ* or *operando* experiment as the latent heat will affect the temperature-sensitive optics in the setup. However, precise control over temperature (and pressure) is of tremendous importance for catalysis in order to mimic industrial conditions. Temperature differences of tens of degrees can cause a completely different product distribution within the Fischer-Tropsch synthesis.^[13,14] As a consequence, an ideal miniaturized reactor allows for local control of temperature (and pressure), without affecting the optics in close proximity.

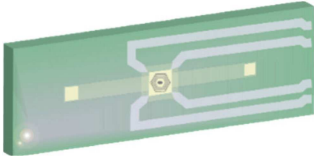
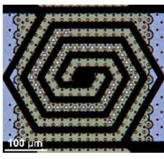
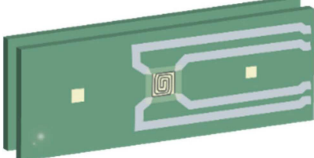
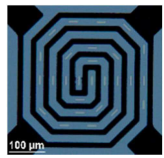
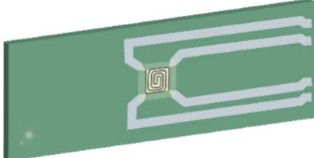
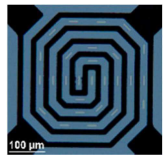
Microelectromechanical systems (MEMS) nano-reactors^[25–28] have been developed over the last decade to satisfy these requirements. For the STXM experiments described in literature,^[3,24] two generations of nano-reactor can be distinguished. Firstly, the monolithic nano-reactor, a single MEMS device with a gas channel that passes between two membranes and a micro-heater spiral on one of the membranes. The

monolithic reactor, described in Figure 1c,^[4] claims to have an accurate and local temperature control (up to 800°C) and can reach up to 14 bar, which comes close to industrially relevant conditions. A second type is the dual-chip nano-reactor, in which two chips are aligned on top of each other to create the gas channel, sealed by O-rings.^[28] In these reactor types, it is much easier to place catalyst particles, but their pressure range is typically limited to 1 bar.

In both types of reactors, the temperature of the heating spiral is monitored and controlled using the temperature-dependent resistance of the micro-heater. Based on the temperature calibration value supplied by the manufacturer, the software's closed-loop feedback system ensures stable temperature by controlling the power output.^[29] However, this temperature value does not reveal information about the distribution of the temperature on the heating spiral as it gives a single average temperature for the whole micro-heater. Furthermore, the nano-reactors were originally designed for transmission electron microscopy (TEM) experiments and thus calibrated to be used in high vacuum.^[30,31] During *in situ* or *operando* STXM experiments, the spiral is no longer in vacuum and therefore the temperature might be lower due to heat dissipation not present in vacuum calibration measurements.

MEMS nano-reactors are widely used in TEM and several attempts to monitor and map the temperature distribution inside the reactor have been made. Vendelbo *et al.*,^[32] explored a quantitative electron energy loss spectroscopy (EELS) method that probes the local temperature of the spiral by measuring the local gas density. Niekietl *et al.*^[33] described local temper-

Table 1. Different nano-reactor designs and corresponding heating spirals used for this study with the applications.

Name	Reactor	Heating spiral	STXM?	Vacuum?	Air?	He/H ₂ flow?
Monolithic nano-reactor			Yes	No	No	No
Nano-reactor Dual Chip			No	Yes	Yes	Yes
Nano-Chip			No	Yes	Yes	No

ature measurements using parallel beam electron diffraction from TEM to map the temperature in MEMS devices, with *in situ* heating experiments in mind. In this method, small gold nanoparticles were distributed over the surface and the temperature-dependent diffraction rings, due to the thermal expansion of the nano-particles, were investigated using selected area electron diffraction. In both cases, a significant temperature gradient was found of 100 °C in vacuum^[32] and up to 320 °C in air.^[33] Although both EELS and electron diffraction experiments show potential for thermometry, the static environment and elaborate calibration procedure limit, in our view, the possibility for *operando* or *in situ* temperature measurements.

Here, we present an alternative method, which relies on the temperature-dependent luminescence of lanthanide-doped nano-microparticles and does not have the above-mentioned restrictions or limitations. Temperature-dependent luminescence of deposited microcrystalline hexagonal NaYF₄:Er³⁺,Yb³⁺,^[34] can be monitored by using a confocal optical microscope. Lanthanide ions are characterized by a partly filled 4fⁿ (n=1–14) shell shielded by filled 5s² and 5p⁶ shells. The inner 4fⁿ shell has a rich energy level structure due to the many different possible distributions for the n electrons over the 14f-orbitals. Optical transitions between the different electronic configurations give rise to efficient sharp line emission. The rich energy level structure, high efficiency and sharpness of the emission make lanthanide luminescence ideal for temperature sensing in different temperature ranges and spectral windows. Here we utilize green Er³⁺ (4f¹¹) emission from the thermally coupled ⁴S_{3/2} and ²H_{11/2} levels. These energy levels are separated by 700 cm⁻¹ and the emission intensity from the higher energy ²H_{11/2} level increases with temperature. The sharpness of the emission lines allows for a very accurate determination of the intensity ratio of emission from the two levels and has been shown to allow for temperature accuracies better than 1 °C.^[35] Temperature readouts can be performed both in vacuum and

gas atmospheres up to at least 600 °C with a spatial resolution of ca. 10 μm. Temperature maps have been obtained for the MEMS nano-reactor under different atmospheres (*i.e.*, vacuum, air and H₂/He) and show temperature gradients of at least 200 °C from the center to the edge of the spiral-shaped heater. In addition, in non-vacuum environment the set temperature (*T*_{set}) is not reached and a temperature offset of 100 °C is observed. Moreover, the observed temperature heterogeneity explains the different reduction behavior found for a Co/TiO₂-based FTS catalyst for individual catalyst particles which are located at different locations in the nanoreactor.

Results and Discussion

During the experiments in this work, several generations of MEMS nano-reactors have been evaluated (see Table 1 and Section S5 for more information). Although the functionalities of the reactors are different, the heating spiral (and therefore the temperature performance) is similar.

Temperature-Dependent Reduction Behavior

Temperature is an important parameter for catalyst performance and preparation. To illustrate this, we performed the reduction of a Co/TiO₂-based FTS catalyst, where we followed the temperature response of individual Co/TiO₂ catalyst particles at different locations within single monolithic nano-reactors by STXM. STXM measurements were performed at the PolLux-X07DA beamline at the Swiss Light Source at the Paul Scherrer Institute (SLS PSI, Villigen, Switzerland). Two reactors were used and are hereafter called (monolithic) reactor-1 and 2, respectively, as they consist of one part. Monolithic reactor-1 had three particles in three different locations (Figure 2a, 1–3),

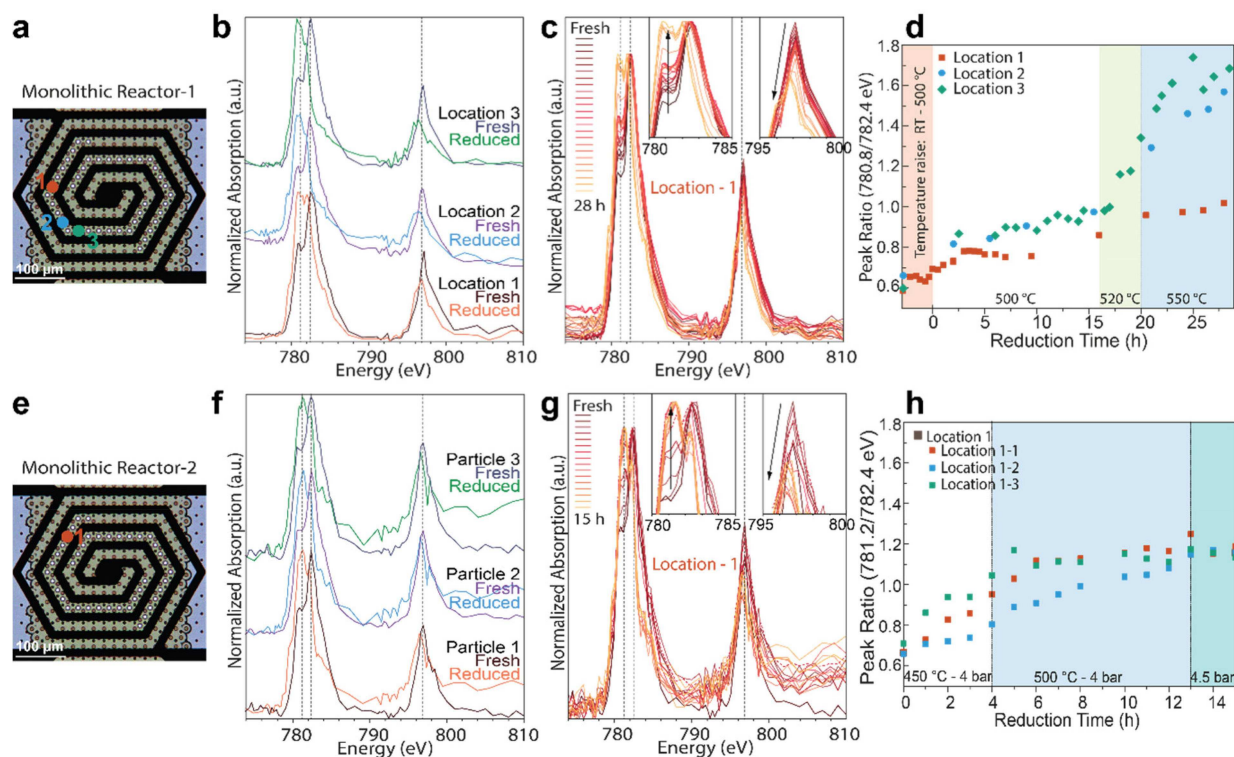


Figure 2. a) The three different locations in monolithic reactor-1. b) X-ray absorption spectra (XAS) of cobalt in the fresh and reduced state of the three catalyst particles for the locations 1–3 in reactor-1. c) Time-dependent XAS of the particle in location 1 from fresh (black) to reduced state (yellow). The peak ratio of 780.8 eV (metallic Co) and 782.4 eV (Co oxides) is plotted against time for the different catalyst particles in d). e) Shows the location of the three particles in monolithic reactor-2. f) X-ray absorption spectra (XAS) of cobalt in the fresh and reduced state of those three catalyst particles. g) Time-dependent XAS of the particle 1 in reactor-2 from fresh (black) to reduced state (yellow). h) Peak ratio as in d) for the three particles.

whereas monolithic reactor-2 had 3 particles in one location (Figure 2e). All the particles are ca. 1 μm in size and consist many cobalt nano-particles supported on a porous TiO_2 support. Upon heating in a H_2 flow, the reduction behavior of the catalyst follows a two-step pathway. The first step consists of the reduction of Co_3O_4 (mixture of Co^{2+} and Co^{3+}) into CoO (Co^{2+}), followed by the reduction from CoO to metallic Co (Co^0 , the second step only starts when all the Co_3O_4 is converted). The X-ray absorption spectroscopy (XAS) data of these different valence states are distinguishable by their $L_{2,3}$ -edges, which makes them an ideal indicator for this study (Figure S3). For reactor-1, the reduction temperature of 500 $^\circ\text{C}$ was reached with a ramp of 10 $^\circ\text{C}/\text{min}$ in a H_2 flow of maximum 1 mL/min and at 4 bar. After 16 h of reduction the temperature was increased to 520 $^\circ\text{C}$ and to 550 $^\circ\text{C}$ after 20 h, with a total reduction time of 28 h. The corresponding Co L-edge XAS spectra of the fresh and reduced samples are shown in Figure 2b, for particles 1–3, and represent the bulk cobalt inside the whole particle. Spectra were taken consecutively by switching between the three different locations and a time-dependent series of location 1 is shown in Figure 2c (the series for locations 2–3 are in the SI). The first spectrum indicates the valence states of Co in the fresh oxide represented by the main peak at 782.4 eV and a shoulder at 780.8 eV. Upon heating in a reducing atmosphere Co is reduced and the valence state of Co is lowered, illustrated in the spectra by an increase of the peak

intensity at 780.8 eV, a peak decrease at 782.4 eV in the L_{3} -edge (left inset of Figure 2c) and a redshift of the L_{2} -edge at ca. 798 eV (right inset of Figure 2c). From the three series of spectra it can be noted that the particles behave differently. Especially the particle at location 1 where the valence state of Co remains higher than the particles in the other two locations. This is visualized in Figure 2d where oxide vs. metallic character (peak ratio 780.8/782.4 eV) is plotted versus reduction time for the three different locations. The orange area before 0 h, represents the ratio of those peaks for location 1, while increasing the temperature from room temperature to 500 $^\circ\text{C}$. The data points in the white region correspond to a reduction temperature of 500 $^\circ\text{C}$ at a pressure of 4 bar H_2 atmosphere. The subsequent temperature rise to and reduction at 520 $^\circ\text{C}$ and to 550 $^\circ\text{C}$ are indicated by the green and blue areas, respectively. With increasing temperature, the ratio for locations 2 and 3 became higher, *i.e.* the particles became more metallic, indicating that they were in fact responsive to temperature changes. However, this response was absent for the particle at location 1, which can be seen in the spectrum after 28 h of reduction, indicating a higher valence state of Co to the others (Figure S3 and 2b).

Different results are obtained when 3 catalyst particles in close proximity are considered (Figure 2e). Here, a reduction temperature of 450 $^\circ\text{C}$ (10 $^\circ\text{C}/\text{min}$ ramp) was reached in a H_2 flow (1 mL/min, 4 bar). After 4 h of reduction, the temperature

was increased to 500 °C and at 13 h the pressure was increased to 4.5 bar with a total reduction time of 16 h.

Figure 2f shows the Co L-edge XAS of the particles at locations 1 and Figure 2g shows a time-dependent series of particle-1 (particles 2 and 3 can be found in the SI). The three particles behave similarly and have a similar Co oxidation state when the reduction was stopped (Figure 2h). The main difference between the experiments in reactor-1 and reactor-2 is the location of the catalyst particles in the heated zone. Therefore, it is likely that the difference in reduction behavior is due to local temperature deviations because of an inhomogeneous temperature distribution. Catalyst particle 2 and 3 in reactor-1 are close to each other (compared to particle 1) and exhibit similar behavior. Since particle 1 is further away, it might experience a different local temperature and therefore show a deviation in reduction behavior. In reactor-2, the particles are all in the same location, resulting in the absence of temperature differences and as a result, there is no difference in reduction behavior observed.

Luminescence Thermometry in Vacuum

To understand the reduction behavior and to test our hypothesis of the inhomogeneous temperature distribution within the heated zone of the nano-reactor, luminescence thermometry was exploited. Upon excitation by a 488 nm laser, microcrystalline NaYF₄ doped with 19% Yb³⁺ and 2% Er³⁺ shows two characteristic emission peaks between 510–570 nm, which change in ratio depending on the temperature (Figure 3).^[36] Here, direct 488 nm excitation in the ⁴F_{7/2} level of Er³⁺ is used rather than infrared (980 nm) excitation in Yb³⁺ which is also frequently used to generate green (upconversion) emission from the ⁴S_{3/2} and ²H_{11/2} levels and explains the presence of the Yb³⁺ co-dopant in the material used.^[35,36] The emission peaks originate from the two thermally coupled levels and at higher

temperatures the emission peaks from the higher energy level ²H_{11/2} increase in intensity.

More information on the principles, experimental details and material used for luminescence thermometry can be found in the Supporting Information Sections S3 and S4. To monitor the temperature in the heating spiral, the NaYF₄ crystals were dispersed in ethanol and drop casted on the spiral, as described and shown in Figure S7. Here, the second type of nano-reactor, *i.e.* the DENSsolutions dual-chip nano-reactor (Table S1), was used, as it proved to be impossible to load the monolithic reactor with the microcrystals without clogging the gas channel. Local temperatures determined from the intensity ratios show that closely spaced ROI's (white rectangles, Figure 4a), have different temperatures. This might be an explanation for the difference in reduction behavior for the Co/TiO₂-based FTS catalyst particles, described in Figure 2.

First, to mimic TEM conditions used in the literature, temperature measurements were performed in vacuum using a Pfeiffer turbopump and a TEM holder. The NaYF₄ crystals were deposited on the heating spiral and the reactor was placed under the microscope (Figure S2). The set temperature (T_{set}) during these measurements was varied between room temperature and 600 °C and kept constant long enough for the temperature to stabilize. The luminescence at different ROI's is shown in Figure 4a and represented by the colored dots (shown here at $T_{\text{set}}=600$ °C). The different colors match different temperatures, as shown in the inset of Figure 4a. A schematic cross-section of the reactor and its environment is given in Figure 4c.

The spiral area was divided into three regions (I, II and III). Here, area I is the area in the center of the spiral, area II is the area of the second ring around the center (full circle minus region I) and area III is the outermost part of the spiral (full circle minus region I and II). The temperatures measured for the different ROI's within an area were averaged and the standard deviation was determined. These measurements have been performed at set temperatures, determined by the electrical resistance feedback of the DENSsolutions software.

Figure 4b shows the temperatures within areas I (blue), II (light-green) and III (dark-green) over time in which the set temperature is slowly increased from room temperature to 600 °C (black dots). The results show that the temperature of the center of the spiral closely matches the set temperature, demonstrating that the MEMS device has an accurate temperature readout via the resistance feedback system. Region II is still close to the set temperature, and when moving away from the center further, the temperature gradually drops. Region III is approximately 200 °C lower in temperature (at $T_{\text{set}}=600$ °C). In fact, luminescence measurements performed at *ca.* 50 μm from the spiral showed no changes with increased heating of the spiral (data not shown here), suggesting that the heating of the spiral is localized to the spiral only. This makes the system ideal for the use in STXM, where the reactor is close to the temperature-dependent optics.

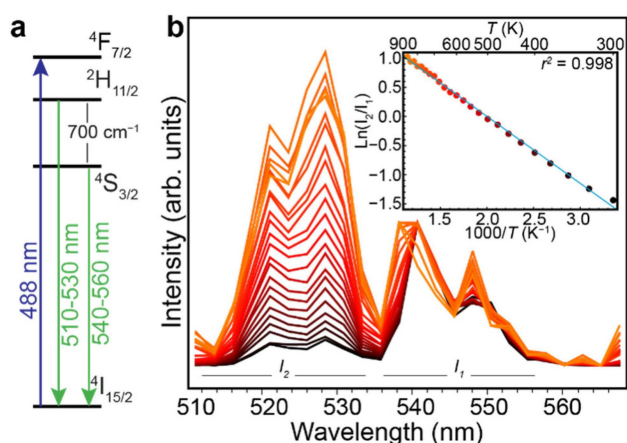


Figure 3. a) Energy levels of Er³⁺, b) temperature-dependent luminescence (510–570 nm) upon increasing the temperature up to 600 °C (black to orange) upon excitation in the ⁴F_{7/2} level (488 nm). The linear correlation of the logarithm of the luminescence intensity ratio [²H_{11/2}–⁴I_{15/2} (I_2)/⁴S_{3/2}–⁴I_{15/2} (I_1)] vs 1000/T is shown in the inset.

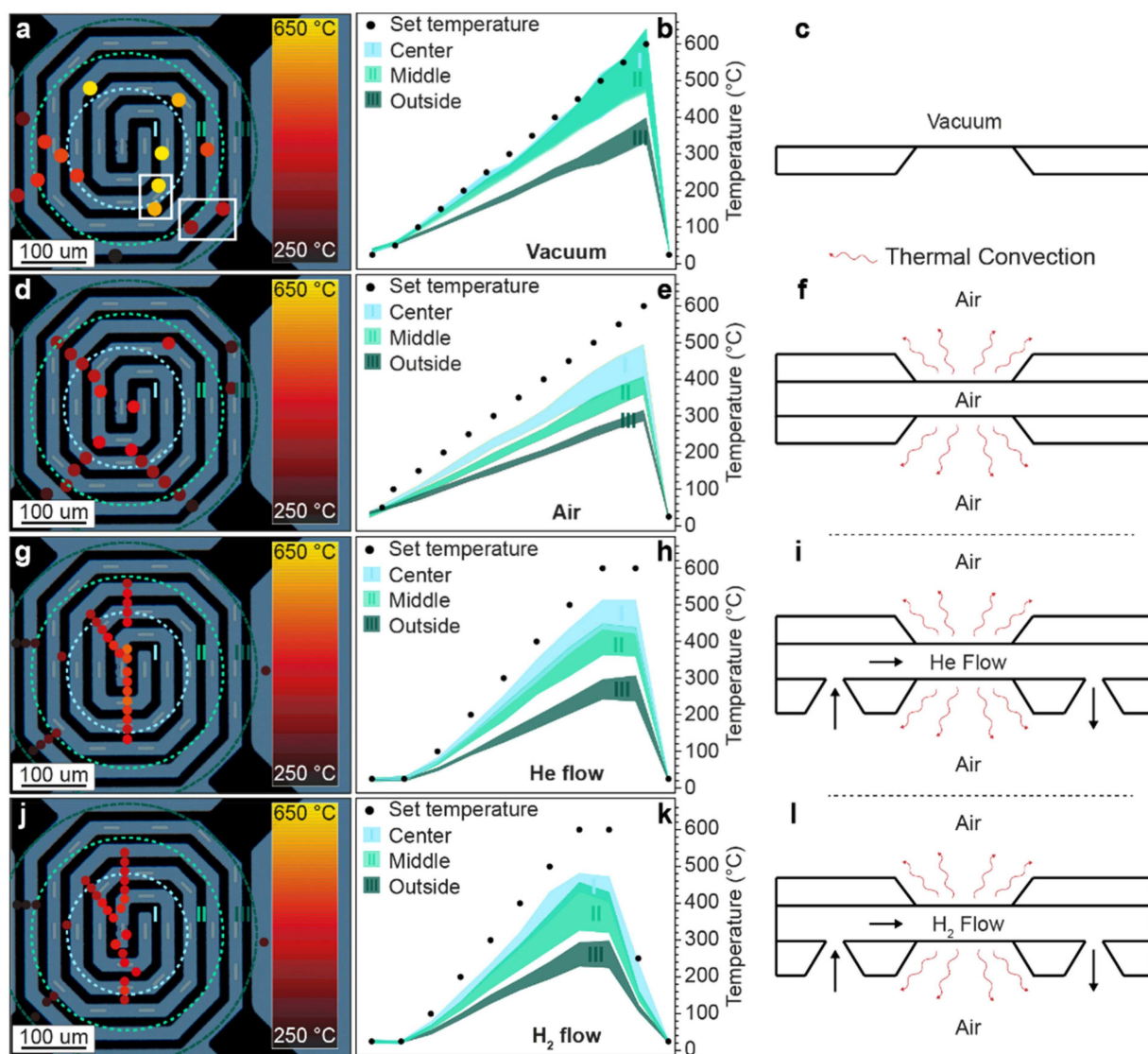


Figure 4. Temperature measurements performed using a confocal microscope to monitor temperature at different spots (which are enlarged for visibility and not to scale) of the heating spiral, a) for experiments performed in vacuum. The white rectangles indicate that even within close proximity, the temperature can be different. The spiral is divided in three regions (I, II, and III) and the average temperature of all spots in a region is plotted versus time, while the set temperature (black dots) was varied (b). c) Schematic representation of the reactor and its environment. d–f) Show the results for experiments performed in air and a schematic cross-section of the reactor and its environment. g–i) Show the results for experiment in a He flow and j–l) for a H₂ flow. The red arrows indicate the possible thermal convection. All shown spots are at $T_{\text{set}} = 600^\circ\text{C}$.

Luminescence Thermometry in Air

The results described in the previous section using luminescence thermometry to map the temperature distribution for a micro-heater in vacuum show good agreement between the temperature in the central region of the heating spiral and the set temperature. Measurements in air are expected to differ due to differences in heat transfer mechanisms. As catalysis does not take place in vacuum, it is important to know the temperature distribution for the micro-heater in a gas atmosphere and therefore the above experiment has been repeated with a dual-chip reactor with air inside. In STXM experiments, the environment external to the reactor is typically 0.33 bar of He gas (to prevent thermal drift of the equipment). To mimic this in the

thermometry measurements, air at atmospheric pressure was used instead of He. In this way, the higher thermal conductivity of the He (155.7 mW/m K at 25 °C^[37]) as compared to air (26.7 mW/m K at 25 °C^[37]) is partially compensated by the higher pressure. Note that this is a different scenario than the situation for which the (TEM) nano-reactor was designed, where the inside pressure is 1 bar, and the outside is vacuum. In the present case (Figure 4f) the surrounding air environment influences the heat transfer by both conduction as well as convection.

The results are shown in Figure 4d and 4e. Again, multiple ROI's have been measured to form a temperature distribution map, as shown by the colored dots in Figure 4d. The same set of temperatures has been evaluated as described before.

However, the luminescence measurements show a much lower readout temperature, reaching only a maximum of approximately 500 °C, which is in line with previous literature.^[32,33] The temperature gradient from the center to the edge of the spiral also changed, with region II now being at considerably lower temperature than the central region I, indicating a decreased homogeneity across the micro-heater. More surprisingly, all regions show a temperature decrease as compared to the situation in vacuum. This was not expected, as software controls the average resistance of these spirals. In other words, if more heat is dissipated through the surrounding gas, the software increases the power until the resistance set point is reached. Therefore, if at the same set temperature region I is colder with respect to the vacuum situation, the temperature in region II and/or III should increase.

The origin of this offset is most likely due to the size of the microcrystalline NaYF₄ temperature sensors (several μm's, Figure S6b). Due to the relatively large size of the sensors, the measured temperature is not confined to the surface of the heating spiral but the average temperature of the microcrystal on top of the heating spiral which will experience a temperature gradient to lower temperatures from the heating spiral surface up. This can explain these lower temperatures. However, in this case, the microcrystalline temperature probe is a good representation of a single catalyst particle used in the reduction experiments, as shown in Figure 2 that will experience a similar temperature gradient. Monitoring the surface temperature at the spiral with smaller (nanosized) temperature probes will be the focus of future work. At the highest temperatures probed thermal stability of fluorides needs to be considered. It is well known that (microcrystalline) fluorides are converted to oxyfluorides at temperatures between 600 and 800 °C in air.^[38,39] This limits the applicability for temperature sensing in air to the presently reported temperatures of ~600 °C. The thermal stability of nanocrystalline NaYF₄ is lower and for high temperature sensing up to 600 °C a protective silica shell around the nanocrystalline NaYF₄ core is needed to allow for temperature sensing up to 600 °C.^[36] In addition to monitoring temperatures at higher pressures,^[40] the temperature range can be increased by using different lanthanide ions and host lattice^[41] showcasing the versatility of luminescence thermometry.

Luminescence Thermometry in a Gas Flow

During a FTS reaction, a gas mixture of H₂ and CO is introduced into the reactor, which induces a flow within the catalytic reactor and which can result in increased heat dissipation. In addition, the composition of the (synthesis) gas can influence the local temperature due to the varying thermal conductivities of gasses (H₂ = 186.6 mW/m K and CO = 25.0 mW/m K^[37]).

In order to investigate the effect of gas flow and gas composition on the nano-reactor performance, an extra set of experiments has been performed in which the nano-reactor was heated to 600 °C under a flow (0.5–1.0 mL/min) of gasses with high thermal conductivities, namely He and H₂. During the heating of the nano-reactor, the temperature of the micro-

heater was determined at several regions of interest as described before. Once more, the area of the heating spiral was divided in three regions (I, II and III) as shown in Figure 4g and 4j for the He and H₂ flow, respectively. The observed temperatures during both flow experiments are very similar, showing a gradient in both cases in which the center (region I) of the heating spiral is hotter than the outside (region III). At the temperature set points of 600 °C, the local temperature in region I only reaches ca. 500 °C, for both He and H₂ flows. The temperature gradient, visualized by the average temperatures in region I, II and III, is shown in Figure 4h and 4k for the He and H₂ experiments, respectively. Figure 4i and 4l, show a schematic representation of the environment for the He and H₂ flow experiments. Although the temperature differences between regions I and II and regions II and III for the H₂ flow experiments are slightly smaller compared to the He flow experiments the overall results are very similar. In both cases the maximum temperature reached is ca. 500 °C at the center of the heating spiral, while the temperature at the outer region only reached ca. 300 °C at the maximum.

The results for both He and H₂ (Figure 4h and k, respectively) are comparable, as expected for the two gasses with similar thermal conductivities (155.7 vs. 186.6 mW/m K). Surprisingly, comparing the He and H₂ flow experiments with the static air experiments show no clear differences. Here, a difference is expected based on the deviating thermal conductivity of air (26.7 mW/m K) and the absence of a flow. This could indicate that the influence of the air external to the reactor is dominant over the influence of the gas inside the nano-reactor. This is important, as it could mean that different gases can be introduced into the nano-reactor without changing the catalyst temperature. Although the results here show no influence of gas composition or flow speed, different reactors with different gas compositions and flow speeds can experience influences on the temperature in larger systems.^[42]

Conclusions

To investigate the temperature homogeneity for micro-heater spirals used in nano-reactors, luminescence thermometry was used for *in situ* measurements using confocal microscopy allowing accurate temperature mapping with ~10 μm resolution. Measurements in vacuum reveal a temperature gradient from the center to the edge of the micro-heater spiral up to 200 °C, resulting in the need for careful thermal evaluation during (catalytic) experiments in MEMS nano-reactors. The observed temperature gradient is in line with previous results in literature and can explain differences in reduction behavior of single Co-based catalyst particles at different locations on the micro-heater during *in situ* X-ray absorption spectroscopy measurements. The role of heat dissipation by gas was investigated by surrounding nano-reactors by different gasses. The results show that upon introduction of a gas, the set temperature is no longer reached. Additional heat dissipation by gasses flowing through the nano-reactor do not seem to influence the temperature distribution as there is no clear trend

with either flow speed or thermal conductivity of the flowed gasses. This indicates that thermal convection at the exterior of the MEMS nano-reactor is the dominant pathway for cooling. The results can successfully explain differences in reduction behavior of Co-based Fischer-Tropsch catalyst particles within a nano-reactor, but the applicability of the developed temperature sensing technique is much broader (e.g. in microfluidics and microelectronics). The temperature discrepancies, uncovered in this work, are most likely due to heat dissipation, but other effects can also play a crucial role in the local temperature, e.g. exo- or endothermic reactions. These effects may also be monitored by high resolution temperature mapping using lanthanide-doped luminescent probes in combination with confocal microscopy.

Acknowledgements

BMW thanks the Netherlands Organization for Scientific Research (NWO) and Shell Global Solutions International B.V. for a CHIPP research grant as well as NWO for a Gravitation program (Netherlands Center for Multiscale Catalytic Energy Conversion (MCEC)). Benjamin Watts (Paul Scherrer Institute) is thanked for the help during the STXM measurements, while Maarten Jongkind, Koen Bossers and Silvia Zanoni (all from Utrecht University, UU) are thanked for their help during the beamtime experiments. Anne-Eva Nieuwelink (UU) is thanked for her help with the confocal microscopy experiments.

Conflict of Interest

The authors declare no conflict of interest.

Keywords: *In Situ* Spectroscopy · Lanthanides · Luminescence Thermometry · Nano-reactor · X-ray Microscopy

- [1] G. T. Withing, F. Meirer, B. M. Weckhuysen, in *XAFS Techniques for Catalysts, Nanomaterials and Surfaces*, (Eds: Y. Iwasawa, K. Asakura, M. Tada) Springer, Berlin, 2017, pp. 167–191.
- [2] F. Meirer, B. M. Weckhuysen, *Nat. Rev. Mater.* **2018**, 3, 324–340.
- [3] E. de Smit, *Nature* **2008**, 456, 222–225.
- [4] E. de Smit, I. Swart, J. F. Creemer, C. Karunakaran, D. Bertwistle, H. W. Zandbergen, F. M. F. de Groot, B. M. Weckhuysen, *Angew. Chem. Int. Ed.* **2009**, 48, 3632–3636; *Angew. Chem.* **2009**, 121, 3686–3690.
- [5] N. E. Tsakoumis, M. Rønning, Ø. Borg, E. Rytter, A. Holmen, *Catal. Today* **2010**, 154, 162–182.
- [6] N. E. Tsakoumis, M. Rønning, Ø. Borg, E. Rytter, A. Holmen, *J. Catal.* **2012**, 291, 138–148.
- [7] I. D. Gonzalez-Jimenez, H. Cats, T. Davidian, M. Ruitenbeek, F. Meirer, Y. Liu, J. Nelson, J. C. Andrews, P. Pianetta, F. M. F. de Groot, B. M. Weckhuysen, *Angew. Chem. Int. Ed.* **2012**, 51, 11986–11990; *Angew. Chem.* **2012**, 124, 12152–12156.
- [8] K. H. Cats, J. C. Andrews, O. Stéphan, K. March, C. Karunakaran, F. Meirer, F. M. F. de Groot, B. M. Weckhuysen, *Catal. Sci. Technol.* **2016**, 6, 4438–4449.
- [9] G. Ertl, H. Knozinger, F. Schuth, J. Weitkamp, Eds. in *Handbook of Heterogeneous Catalysis*, Weinheim, Wiley-VCH, 2008.
- [10] S. E. Colley, R. G. Copperthwaite, G. J. Hutchings, S. P. Terblanche, M. M. Thackeray, *Nature* **1989**, 339, 129–130.
- [11] Z.-P. Liu, P. Hu, *J. Am. Chem. Soc.* **2002**, 124, 11568–11569.
- [12] A. Y. Khodakov, W. Chu, P. Fongarland, *Chem. Rev.* **2007**, 107, 1692–1744.
- [13] H. Schulz, *Appl. Catal. A* **1999**, 186, 3–12.
- [14] A. Y. Krylova, *Solid Fuel Chem.* **2014**, 48, 22–35.
- [15] P. A. U. Aldana, F. Ocampo, K. Kobl, B. Louis, F. Thibault-Starzyk, M. Daturi, P. Bazin, S. Thomas, A. C. Roger, *Catal. Today* **2013**, 215, 201–207.
- [16] J. Lee, *J. Catal.* **2015**, 330, 19–27.
- [17] L. Lemaitre, A. Berliet, S. Maury, M. Rivallan, *Catal. Today* **2017**, 283, 172–175.
- [18] N. E. Tsakoumis, *Catal. Today* **2013**, 205, 86–93.
- [19] A. Rochet, V. Moizan, F. Diehl, C. Pichon, V. Briois, *Catal. Today* **2013**, 205, 94–100.
- [20] A. Rochet, V. Moizan, F. Diehl, C. Pichon, V. Briois, *J. Phys. Chem. C* **2015**, 119, 23928–23942.
- [21] D. K. Lee, J. H. Lee, S. K. Ihm, *Appl. Catal.* **1988**, 36, 199–207.
- [22] A. M. Saib, D. J. Moodley, I. M. Ciobic, M. M. Hauman, B. H. Sigwebela, C. J. Weststrate, J. W. Niemantsverdriet, J. van de Loosdrecht, *Catal. Today* **2010**, 154, 271–282.
- [23] D. J. Moodley, J. van de Loosdrecht, A. M. Saib, M. J. Overett, A. K. Datye, J. W. Niemantsverdriet, *Appl. Catal. A* **2009**, 354, 102–110.
- [24] I. K. van Ravenhorst, C. Vogt, H. Oosterbeek, K. W. Bossers, J. G. Moya-Cancino, A. P. Van Bavel, A. M. J. van der Eerden, D. Vine, F. M. F. de Groot, F. Meirer, B. M. Weckhuysen, *Angew. Chem. Int. Ed.* **2018**, 57, 11957–11962; *Angew. Chem.* **2018**, 130, 12133–12138.
- [25] J. F. Creemer, S. Helveg, G. H. Hoveling, S. Ullmann, A. M. Molenbroek, P. M. Sarro, H. W. Zandbergen, *Ultramicroscopy* **2008**, 108, 993–998.
- [26] E. A. Ring, N. de Jonge, *Microsc. Microanal.* **2010**, 16, 622–629.
- [27] J. F. Creemer, F. Santagata, B. Morana, L. Mele, T. Alan, E. Iervolino, F. Pandraud, P. M. Sarro, *Proc. IEEE Int. Conf. Micro Electro Mech. Syst.* **2011**, 1103–1106.
- [28] H. H. Pérez Garza, D. Morsink, J. Xu, M. Sholkina, Y. Pivak, M. Pen, S. van Weperen, Q. Xu, *Micro Nano Lett.* **2017**, 12, 69–75.
- [29] J. T. van Ommen, M. Zakhosheva, R. G. Spruijt, M. Sholkina, H. H. Pérez Garza, *Ultramicroscopy* **2018**, 192, 14–20.
- [30] M. Zhang, E. A. Olson, R. D. Twisten, J. G. Wen, L. H. Allen, I. M. Robertson, I. Petrov, *J. Mater. Res.* **2005**, 20, 1802–1807.
- [31] L. Mele, S. Konings, P. Dona, F. Evertz, C. Mitterbauer, P. Faber, R. Schampers, J. R. Jinschek, *Microsc. Res. Tech.* **2016**, 79, 239–250.
- [32] S. B. Vendelbo, P. J. Kooyman, J. F. Creemer, B. Morana, L. Mele, P. Dona, B. J. Nelissen, S. Helveg, *Ultramicroscopy* **2013**, 133, 72–79.
- [33] F. Niekiel, S. M. Kraschewski, J. Müller, B. Butz, E. Spiecker, *Ultramicroscopy* **2017**, 176, 161–169.
- [34] L. Aarts, B. M. van der Ende, A. Meijerink, *J. Appl. Phys.* **2009**, 106, 5–10.
- [35] X. Wang, Q. Liu, Y. Bu, C.-S. Liu, T. Liu, X. Yan, *RSC Adv.* **2015**, 5, 86219–86236.
- [36] R. G. Geitenbeek, P. T. Prins, W. Albrecht, A. van Blaaderen, B. M. Weckhuysen, A. Meijerink, *J. Phys. Chem. C* **2017**, 121, 3503–3510.
- [37] D. R. Lide in *CRC Handbook of Chemistry and Physics*, 85th ed. Boca Raton, CRC Press, 2005.
- [38] M. J. J. Lammers, G. Blasse, *Phys. Status Solidi B* **1985**, 127, 663–671.
- [39] X. Cheng, X. Ma, H. Zhang, Y. Ren, K. Zhu, *Physica B* **2017**, 521, 270–274.
- [40] M. Runowski, A. Shyichuk, A. Tyminski, T. Grzyb, V. Lavín, S. Lis, *ACS Mater. Interfaces* **2018**, 10, 17269–17279.
- [41] R. G. Geitenbeek, B. B. V. Salzmänn, A.-E. Nieuwelink, A. Meijerink, B. M. Weckhuysen, *Chem. Eng. Sci.* **2019**, 198, 235–240.
- [42] R. G. Geitenbeek, A. E. Nieuwelink, T. S. Jacobs, B. B. V. Salzmänn, J. Goetze, A. Meijerink, B. M. Weckhuysen, *ACS Catal.* **2018**, 8, 2397–2401.

Manuscript received: May 31, 2019
 Revised manuscript received: August 24, 2019
 Accepted manuscript online: August 26, 2019
 Version of record online: October 2, 2019